Reactor field reconstruction from sparse and movable sensors using Voronoi tessellation-assisted convolutional neural networks

Helin Gong,[1] Han Li,[1] Dunhui Xiao,[2] and Sibo Cheng[3]

[1] *Paris Elite Institute of Technology, Shanghai Jiao Tong University, Shanghai 200240, China*
[2] *School of Mathematical Sciences, Tongji University, 200092 Shanghai, China*
[3] *Data Science Institute, Department of computing, Imperial College London, London, SW7 2AZ, UK* *

The aging of operational reactors leads increased mechanical vibrations of reactor internals. The vibration of the in-core sensors near their nominal locations is a new issue for the neutronic fields reconstruction. Current field reconstruction methods fail to handle spatially moving sensors. In this work, we proposed a Voronoi tessellation techinque in combination with convolutional neural networks (V-CNN) to handle this challenge. The observations from movable in-core sensors are projected to the same global field structure, this projection is achieved with Voronoi tessellation, holding the magnitude and location information of sensors. The general convolutional neural networks were used to learn the map from observations to the global field. The proposed method is able to reconstruct the multi-physics fields (e.g., the fast flux, thermal flux and power rate) using observations from single field (e.g., thermal flux). Numerical tests based on IAEA benchmark proved its potential for real engineering usage, particularly, within an amplitude of 5 cm around nominal locations, the field reconstruction leads to average relative errors below 5% and 10% in L_2 norm and L_∞ norm, respectively.

Keywords: Voronoi tessellation; Field reconstruction; Nuclear reactors; Reactor physics; On-line monitoring

I. INTRODUCTION

Since its advent in the 1950s, nuclear energy plays a crucial role in meeting world energy needs and is also an important component of clean energy today. Nuclear energy is mainly generated through nuclear reactors, which are generally designed to operate for 30 to 40 years and can last even longer with license renewals. Based on data from the Power Reactor Information System (PRIS), among the total of 437 reactors, 289 reactors have been in operation for more than 30 years [1]. In other words, more than 60% of the current nuclear reactors are facing aging issues. As a consequence, reactor operational problems or anomalies are expected to be more frequent. The aging of operational reactors also leads to increased mechanical vibrations of reactor internals such as core barrel, control rods, in-core instruments and more specifically fuel assemblies, or other vibrations such as flow blockage, coolant inlet perturbations [2–6].

Various reactor core monitoring techniques aim to address these challenges, mainly based on using the observations of neutron flux acquired by in-core and ex-core instrumentation, combining numerical simulations. Such techniques and systems include, but are not limited to CORTEX [7], BEACON [8], RAINBOW [9], etc. We refer the readers to [10] a detail overview of the reactor core monitoring techniques. The process that combining observed data in the core and the simulation data is generally called field reconstruction [11, 12], with the main goal to infer the neutronic field in the core, thereafter the safety related parameters can be calculated, such as enthalpy rise hot channel factor (FdH), peak heat flux hot channel factor (FQ), linear power density of fuel rods (LPD) and deviation from nucleate boiling ratio (DNBR), etc.

On the key algorithms for field reconstruction, one prototype is data assimilation that originally arises in earth sciences including meteorology and oceanography [13]. Data assimilation framework allows combining observations and models in an optimal and consistent way, including information about their uncertainties [14–16]. It has been applied in several studies in nuclear engineering fields [9, 17–21] for field reconstruction in a unified formalism. Another framework is data assimilation with reduced basis, which also has extensive research in recent years, see [22–32]. In a word, many efforts in data assimilation aim to improve the accuracy, efficiency and robustness of physical field reconstruction. We refer the interested readers to the review paper [33].

On the other hand, the location of sensors affects the accuracy and robustness of the reconstructed field, thus an important aspect is to study the optimization of sensor placement. In [22], the authors proposed the so called Generalized Empirical Interpolation Method (GEIM) [34] to select the quasi-optimal sensor locations in the framework of data assimilation and reduced basis. Subsequently, validation was conducted on three types of reactors in operation at Électricité de France (EDF). In [35], the authors applied simulated annealing to optimize the placement of fixed in-core detectors, using the variance-based and information entropy-based methods to define the objective function. Recently, clustering, such as the K-means algorithm is used to optimize the in-core detector locations for flux mapping in AHWR [36, 37]. In recent work, greedy algorithm is used to optimize sensor locations on a grid, adhering to user-defined constraints, in building the nuclear digital twins based on the Transient Reactor Test facility (TREAT) at Idaho National Laboratory (INL) [38]. All these methods attempt to optimize the placement of the in-core detectors in a heuristic manner, and they are limited to a fixed sensor arrangement as that used in a training process; however, little research has been done on algorithms for handling detector vibrations.

The vibration of the in-core sensors near their nominal locations is a new issue, which may be caused by the aging of operational reactors. A typical limitation stems from the

* Corresponding author, sibo.cheng@imperial.ac.uk

fact that all methods mentioned above fail to handle spatially moving sensors. Recently, the work in [39] opens a new pathway toward the practical use of neural networks for global field estimation, considering sensors could be in motion and could become online or offline over time. In that work, the authors used the Voronoi tessellation [40] to obtain a structured-grid representation from sensor locations, thereafter the convolutional neural networks (CNN) can be used for building the map from movable sensors to the physical field. Inspired by that work, we adapted the framework to the application of field reconstruction in nuclear reactors, which is able to take the vibration of sensors into consideration when reconstructing neutronic fields.

The rest of this paper is organized as follows. In Section II, we give a detailed description of the methodology for field reconstruction with movable sensors using Voronoi tessellation in combination with convolutional neural networks (V-CNN). In Section III, we present the physical model and the detailed process to reconstruct the neutronic field. Section IV illustrates the numerical results, in which various error metrics have been presented to evaluate the performance of the method. Finally, we give a brief conclusion and further works in Section V.

II. METHODOLOGY FOR FIELD RECONSTRUCTION WITH MOVABLE SENSORS

Our goal is to reconstruct a two-dimensional neutronic field $\in \mathbb{R}^{n_x \times n_y}$ in the reactor core domain $\Omega \in \mathbb{R}^2$ from sparse and limited in-core sensor observations $y \in \mathbb{R}^{n_{obs}}$ at locations r_{y_i}, $i = 1, ..., n_{obs}$. Here n_{obs} indicates the number of in-core sensor observations and n_x and n_y denote the number of grid points in the horizontal (x) and vertical (y) directions on a high-resolution field, respectively. The challenge here is to handle movable sensors at their nominal locations over the field. The field reconstruction process should be performed with only a single machine learning model to avoid retraining when sensors move from their nominal locations. This is achieved through two key processes, i.e.,

(i) a partition method using Voronoi tessellation which is able to tolerate the local perturbations of sensor locations;

(ii) a machine learning framework that maps the observations to the global physical field in the same structure.

We remark here that, considering the sensors in the core of a reactor are fixed, such as self-power neutron detectors (SPND), we only consider cases of sensors vibrate near their fixed positions, rather than significant movement in the whole domain over time. The latter corresponds to the cases referred to [39].

We illustrate in Fig. 1 the framework, i.e., Voronoi tessellation-assisted convolutional neural networks (V-CNN) for neutronic fields reconstruction, and give a detailed description of each component in the following sections.

A. Voronoi tessellation for spatial domain partitions

To achieve the goal of the reconstruction using movable sensors, the Voronoi tessellation is a key step that maps the observations to the whole spatial domain. For a given space Ω, which is generally in 2D, a set of points $\{r_i,\ i = 1, ..., n_{obs}\} \in \Omega$. The tessellation approach optimally partitions the given space Ω into n_{obs} regions $G = \{g_1, g_2, ..., g_{n_{obs}}\}$ using boundaries determined by the measure d among the given points. Using the measure d, Voronoi tessellation can be expressed as

$$g_i = \{r \in \Omega \mid d(r, r_i) < d(r, r_j),\ j \neq i\}. \tag{1}$$

In this article, the Euclidean measure is used and the Voronoi boundaries between points are their bisectors. Fig. 2 illustrates an example of 81 points and the related Voronoi partitions in Euclidean measure. The Voronoi tessellation provides a convenient way to project the sparse sensor observations to the global physical field, thus leaning the map from sparse observations to the global field using CNN is possible. More importantly, this partition process is able to tolerate the local perturbations of sensor locations. For more details on the mathematical theory of Voronoi tessellation, we refer the readers to the studies such as [40–43].

B. Input and output of the machine learning model

To reconstruct the physical field using machine learning method, we utilize the following process to prepare the input data of model.

(i) Determine the sensor locations r_{y_i}, $i = 1, ..., n_{obs}$ in the reactor core. r_{y_i} may vibrate from its nominal location $r_{y_i}^{nominal}$, and we have $r_{y_i} = r_{y_i}^{nominal} + \delta r_{y_i}$, where δr_{y_i} is a small quantity caused by vibration.

(ii) Calculate the Voronoi tessellation $s_i \in \mathbb{R}^{n_x \times n_y}$ using r_{y_i}, $i = 1, ..., n_{obs}$. The Voronoi tessellation first partitions the reactor domain Ω into n_{obs} regions $G = \{g_1, ..., g_{n_{obs}}\}$ with $\Omega = \cup_{i=1}^{n_{obs}} g_i$, each region g_i contains one sensor located at r_{y_i}, and s_i is defined as follows

$$s_i(r) = \begin{cases} 1 & \text{if } r \in g_i \\ 0 & \text{otherwise} \end{cases}. \tag{2}$$

(iii) Prepare the Voronoi mask field $\phi_m \in \mathbb{R}^{n_x \times n_y}$ using Voronoi tessellation s_i, $i = 1, ..., n_{obs}$. The element $\phi_m(r)$ satisfies

$$\phi_m(r) = y_{r_i}\ , \quad \text{if } r \in g_i. \tag{3}$$

The Voronoi mask field ϕ_m and the related target neutronic field ϕ_n are provided to a machine learning model $\mathcal{F}_\delta$, such that $\mathcal{F}_\delta : \phi_m \longmapsto \phi_n$, where δ means that the model is trained for a given δ. The final output of the model is then denoted

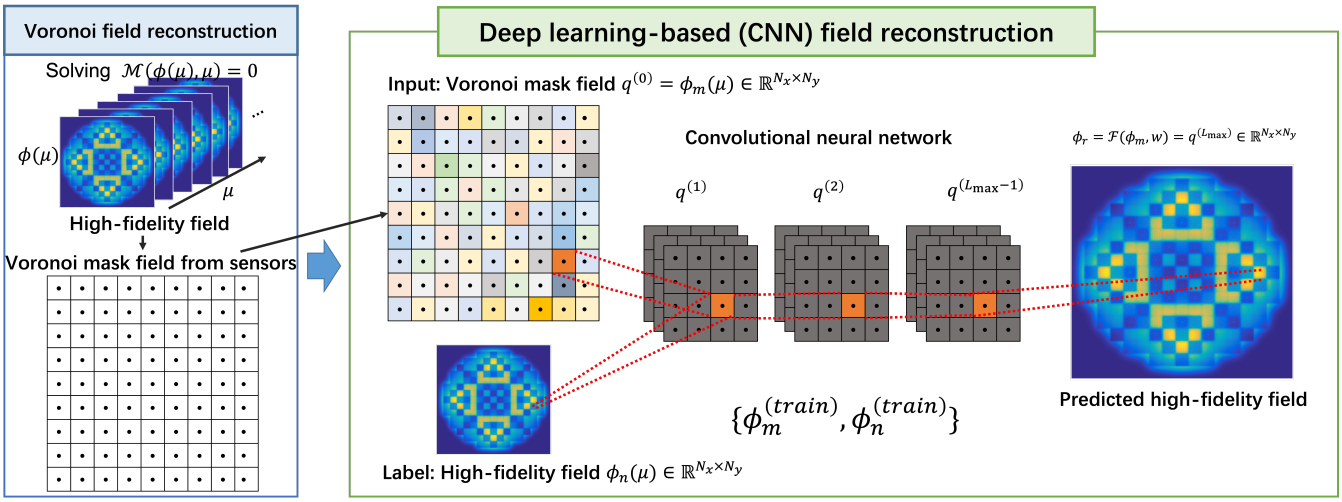

Fig. 1. Voronoi tessellation-assisted convolutional neural networks for neutronic fields reconstruction from discrete sensor locations in a two-dimensional reactor core. The input Voronoi field is constructed from 81 sensors from each center of fuel assembly. The Voronoi field is then fed into a convolutional neural network with the Voronoi mask field ϕ_m, and the output of CNN is the reconstructed field ϕ_r. In the mask field, a grid with a sensor i (black circle) has a value of $\phi_{m,i}$, which reflects the detected value of the underlying field at site.

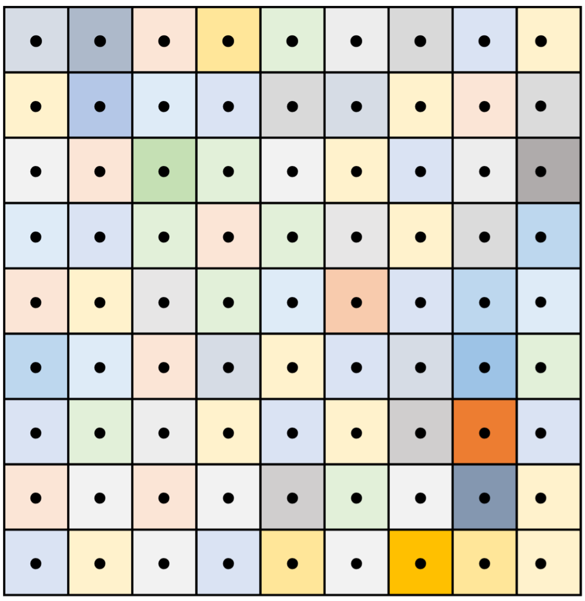

Fig. 2. An example of 81 points and the related Voronoi tessellation using Euclidean measure.

by $\phi_r = \mathcal{F}_\delta(\phi_m)$, where the subscript '$r$' presents the reconstructed neutronic field. With the specified input vector holding the observed value and the position information of the sensors, the proposed model can deal with arbitrary sensor locations and arbitrary numbers of sensors.

Note here that the perturbations of sensor locations and whether this would have an impact on the effectiveness of the network is also investigated in this work. The typical amplitude δ of the vibration of sensors in a reactor core is less than $1cm$ [6], to go further, we investigated the cases of $\delta = 1cm, 3cm$ and $5cm$, and the effects of the number and location of sensors in these scenarios will be illustrated in numerical results section.

To construct the training set $\{\phi_m^{(\text{train})}, \phi_n^{(\text{train})}\}$ and test set $\{\phi_m^{(\text{test})}, \phi_n^{(\text{test})}\}$ for the learning process, a physical model of the underlying problem

$$\mathcal{M}(\phi(\mu), \mu) = 0, \tag{4}$$

is solved numerically. Here $\mu \in \mathcal{D} \subset \mathbb{R}^p$ is the p-dimensional parameter of the model and $\mathcal{D}$ is the feasible parameter domain. The training set and test set are accumulated by solving Eq. (4) over a discrete set $\mathcal{D}^{(\text{discrete})}$ which is representative of $\mathcal{D}$.

C. Learning the map using convolutional neural networks

Once the input data is prepared for the model, a CNN model can be used to learning the map from observations to the field, in the same way as handling images [44–46]. In this work, the channel of CNN is set to one, and for each layer the process to extract key features of input data through filtering operations can be expressed as

$$q_{ijm}^{(l)} = \sigma\Big(\sum_{p=0}^{H-1}\sum_{c=0}^{H-1} q_{i+p-C,j+c-C,m}^{(l-1)} h_{pcm} + b_m\Big). \tag{5}$$

Here $C = \text{floor}(H/2)$, $q^{(l-1)}$ and $q^{(l)}$ are the input and output data at layer l, respectively; h_{pcm} presents a filter of size $H \times H$ and b_m is the bias. l_{max}, H and m denote the number of layers, the size of filter and the number of filters, respectively. The output of each filter operation is fed to an activation function $\sigma(\cdot)$ as the output of neurons. In this work, we chose the rectified linear unit (ReLU) $\sigma(z) = \max(0, z)$

as the activation function [47]. We use the ADAM optimizer with an early stopping criterion for training, and a threefold cross-validation is used [48–50]. Furthermore, the L_2 norm is used to measure the error in the learning process. The detail parameters of the CNN used in this work are summarized in Table 1.

We fed the Voronoi mask field $\phi_m \in \mathbb{R}^{n_x \times n_y}$ to the model $\mathcal{F}$, i.e., $q^{(0)} = \phi_m$, and the output of model is a high-resolution neutronic field $q^{(l_{max})}$. The learning process can be formulated as

$$w = \arg\min_{w} \|q - \mathcal{F}(\phi_m, w)\|_2, \tag{6}$$

where w denotes model parameters, specifically filters of CNN in this work. Once the training process is finished, the field reconstruction can be achieved by feeding the observations y to the model $\mathcal{F}$, i.e., $\phi(y) = \mathcal{F}(\phi_m(y), w)$.

Table 1. Parameter settings of CNN.

Layers l_{max}	Hidden layers	Filter size H	Number of filters m	Learning rate of ADAM	Resolution $n_x \times n_y$
9	7	8	48	0.0001	171×171

III. APPLICATION TO NEUTRONIC FIELD RECONSTRUCTIONS

A. Physical model

In this section, we test the reconstruction method in nuclear reactor core. We consider a typical benchmark in nuclear reactor physics, i.e., the 3D IAEA benchmark problem [51]. This benchmark was prepared by the computational benchmark problems committee of the mathematics and computation division of the American nuclear society. The reason for choosing this benchmark is that this benchmark is adapted from realistic reactors, and the geometry and the composition are much more complex than single region or two regions problems. Once this test is passed, the next step will be to test the method directly based on real reactor calculations

For algorithm testing purpose, we use the 2D IAEA case which represents the midplane $z = 190$ cm of the 3D IAEA benchmark, see [51, page 437] for a detail description. The 2D geometry of the reactor is shown in Figure 3, where only one quarter is given because the rest can be inferred from symmetry along the x and y axes. This one quarter is denoted by Ω and it is composed of four subregions of different physical properties: the first three subregion form the core domain $\Omega_{1,2,3}$, while the fourth subregion is the reflector domain Ω_4. Certain Newman boundary conditions are satisfied on the x and y axes considering symmetry, and the zero boundary condition is satisfied on the external border, see Fig. 3.

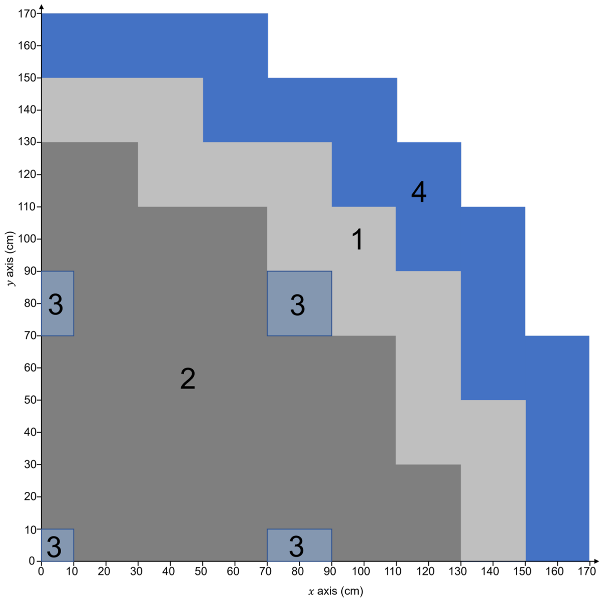

Fig. 3. Geometry of 2D IAEA nuclear core, upper octant: region assignments, lower octant: fuel assembly identification (from [51]).

The neutron fields are composed of fast flux and thermal flux, i.e., $\phi = (\phi_1, \phi_2)$ are modeled by two-group neutron diffusion equation with suitable boundary conditions. The fluxes are the solution to the following eigenvalue problem (see [52, 53]). To be precise, the flux ϕ satisfies the following eigenvalue problem: Find $(\lambda, \phi) \in \mathbb{C} \times L^\infty(\Omega) \times L^\infty(\Omega)$, s.t.

$$\begin{cases} -\nabla\left(D_1 \nabla \phi_1\right) + \left(\Sigma_{a,1} + \Sigma_{1\to 2} + D_1 B_{z1}^2\right)\phi_1 = \dfrac{1}{\lambda}\nu\Sigma_{f,2}\phi_2 \\ -\nabla\left(D_2 \nabla \phi_2\right) + (\Sigma_{\mathrm{a},2} + D_2 B_{z2}^2)\phi_2 = \Sigma_{1\to 2}\phi_1 \end{cases}, \tag{7}$$

with the zero boundary condition $\phi_i = 0,\ i = 1, 2$ on external border $\partial\Omega$ and Newman boundary conditions $\partial(\phi_i)/\partial(n) = 0,\ i = 1, 2$ on axises. The generated nuclear reactor rate is $P = \nu\Sigma_{f,1}\phi_1$, which reflect the power distribution over the core. The following parameters are involved in the above equation:

- D_i: the diffusion coefficient of group i with $i \in \{1, 2\}$;
- $\Sigma_{a,i}$: the macroscopic absorption cross section of group i;
- $\Sigma_{1\to 2}$: the macroscopic scattering cross section from group 1 to 2;
- $\Sigma_{f,i}$: the macroscopic fission cross section of group i;
- ν: the average number of neutrons emitted per fission.

The axial buckling $B_{zi}^2 = 0.8 \cdot 10^{-4}$ for all regions and energy groups. The nominal values of the coefficients in the diffusion model (7) are listed in Section III A.

Table 2. Parameter values of the 2D IAEA benchmark problem.

Region	D_1 (cm)	D_2 (cm)	$\Sigma_{1\to2}$ (cm^{-1})	$\Sigma_{a,1}$ (cm^{-1})	$\Sigma_{a,2}$ (cm^{-1})	$\nu\Sigma_{f,1}$ (cm^{-1})	$\nu\Sigma_{f,2}$ (cm^{-1})	Material
Ω_1	1.50	0.40	0.02	0.01	0.080	0.00	0.135	Fuel 1
Ω_2	1.50	0.40	0.02	0.01	0.085	0.00	0.135	Fuel 2
Ω_3	1.50	0.40	0.02	0.01	0.130	0.00	0.135	Fuel 2 + Rod
Ω_4	2.00	0.30	0.04	0.00	0.010	0.00	0.000	Reflector

* The axial buckling $B^2_{zi} = 0.8 \cdot 10^{-4}$ for all regions and energy groups.

Under some mild conditions of the parameters, the maximum eigenvalue $\lambda_{\max}$ is real and strictly positive (see [54, Chapter XXI]). The associated eigenfunction ϕ is also real and positive at each point $\mathbf{x} \in \Omega$ and it is the flux of interest. In neutronics, it is customary to use the inverse of $\lambda_{\max}$, that is called the multiplication factor

$$k_{\text{eff}} := \frac{1}{\lambda_{\max}}. \tag{8}$$

Here, for each parameter setting, k_{eff} is determined by the solution to the eigenvalue problem (7). The maximum eigenvalue $\lambda_{\max}$ can be computed based on the well-known power method (see [52]). In this work, the Freefem++ [55] is used to solve the 2D IAEA benchmark problem. The spatial approximation uses $\mathbb{P}_1$ finite elements with a grid of size $h = 1$ cm, thus the resolution of the field is $n_x \times n_y = 171 \times 171$.

B. Field reconstruction

To simulate the variation of the neutronic fields with respect to parameter variations, we take the parameters in Section III A as uncertain parameters. To be precise, we assume that

$$\mu = (\mu_1, \mu_2, ..., \mu_n) \in \mathcal{D} = [\mu_{i,nominal} \cdot 0.8, \mu_{i,nominal} \cdot 1.2]^n \tag{9}$$

where $\mathcal{D}$ is the parameter domain. We randomly generate 10000 samplings of μ in $\mathcal{D}$, and solve Eq. (7) to get a collection of 10000 samples of neutronic fields $\mathcal{M} = \{\phi_1(\mu), \phi_2(\mu), P(\mu) \mid \mu \in \mathcal{D}\}$. Among then, 8000 samples are used for training, 1000 samples are used for validation and 1000 for testing. In this work, we train three CNN models with the same input data, i.e., the thermal flux ϕ_2 which is measurable with in-core detectors, and the output fields are the fast flux ϕ_1, the thermal flux ϕ_2 and the reaction rate P, see Fig. 4 for a schematic diagram.

To synthesize observations, we assume in the center of each assembly, there exists an in-core sensor to acquire the thermal flux. We further assume that these sensors can move in a local square with width δ cm, centered at the center of each assembly. In this work, we will brought out the numerical tests for the cases $\delta = 1, 3, 5$ cm, to investigate the effect of different levels of vibration of sensors. This means that the observations are generated randomly from the windows of width δ centered at their nominal locations, see Fig. 5. Then the model $\mathcal{F}$ is trained based on the set $\mathcal{M}$, a schematic diagram for the training process can be found in Fig. 1 and Fig. 4.

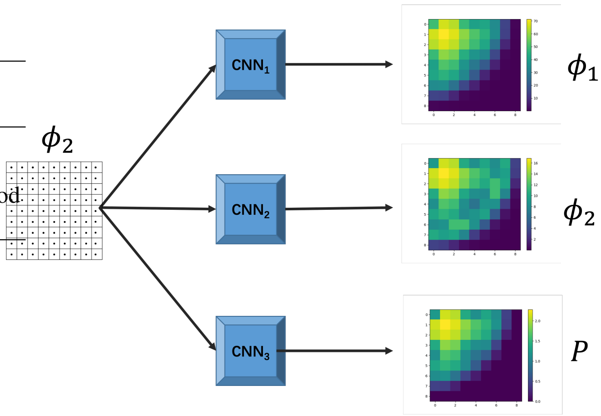

Fig. 4. A schematic diagram for the reconstruction the neutronic fields.

C. Error metrics

Before we present numerical results, we define several metrics to evaluate the quality of various field reconstructions. The normalized root-mean-square residual of the difference of the reconstruction ϕ_r and the test field ϕ_t is

$$e_2(\phi) := \frac{\|\phi_r - \phi_t\|_2}{\|\phi_t\|_2}. \tag{10}$$

In nuclear engineering domain, the error of the reconstructed field in L_∞ is another import metric, which reflects the worst case for each reconstruction.

$$e_\infty(\phi) := \frac{\|\phi_r - \phi_t\|_{L_\infty}}{\|\phi_t\|_{L_\infty}}. \tag{11}$$

The total average root-mean-square residual and the standard deviation over the given test set $\mathcal{M}$ are defined as

$$\begin{array}{ll} E(e_\chi(\phi)) & := \text{average}_{\phi\in\mathcal{M}}(e_\chi(\phi)) \\ STD(e_\chi(\phi)) & := \text{standard deviation}_{\phi\in\mathcal{M}}(e_\chi(\phi)) \end{array}, \tag{12}$$

where χ denotes L_2 or L_∞ norm.

Furthermore, the average assembly field (fluxes and power rate) and the related errors are also investigated. The average assembly power is defined as

$$\phi_{ass,k} = \frac{1}{v_k} \int_{v_k} \phi dv, \tag{13}$$

where ϕ denotes ϕ_1, ϕ_2 or P, v_k denotes the volume of the k-th subassembly, and k designates the fuel assemblies as shown in lower octant of Fig. 3. The average error $e_2(\phi_{ass})$ and maximum relative error $e_\infty(\phi_{ass})$ and the related average $E(e_\chi(\phi_{ass}))$ and standard deviation $STD(e_\chi(\phi_{ass}))$ of the errors over the given test set $\mathcal{M}$ can also be defined in a similar way.

To this end, we introduce the structural similarity (SSIM) [56] index to measure the field reconstruction. Contrary to the general L_2 error, the SSIM index provides a measure of the similarity by comparing two images based on luminance similarity, contrast similarity and structural similarity information.

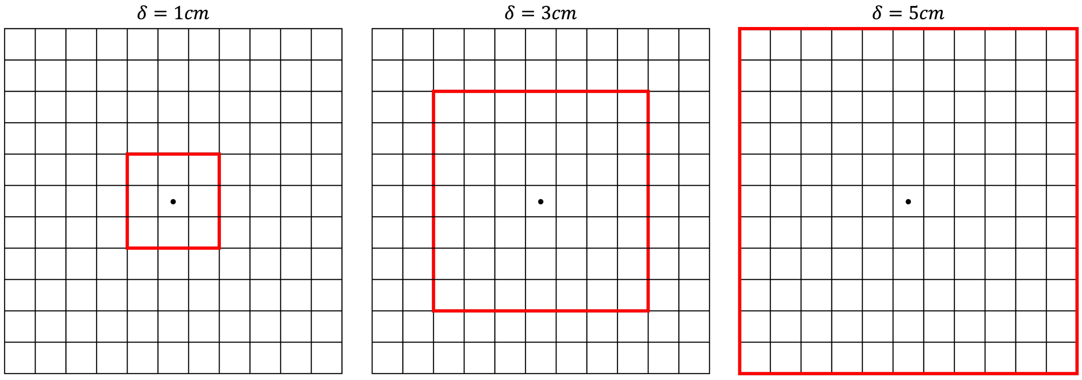

Fig. 5. Different amplitudes of vibrations of a sensor near the nominal location in an assembly.

IV. NUMERICAL RESULTS

We have finished to describe the methodology for field reconstruction with movable sensors using CNN in Section II and presented a detailed process for neutronic fields reconstruction based on a typical benchmark nuclear engineering domain in Section III. In this section, we illustrate the numerical performance of the proposed method.

A. Performance for the benchmark problem

We first show in Fig. 6 the error distribution of the reconstructed fields for different vibration amplitudes, i.e., $\delta = 1, 3, 5$ cm for the 2D IAEA benchmark problem. The reconstruction of ϕ_1 using observations from ϕ_2 shows the best performance than the reconstruction of ϕ_2 and P. Furthermore, with the amplitude of the vibration becoming larger, i.e., δ varies from 1 cm to 5 cm, the reconstructed error also increases. The largest error appears around the interface of the fuel and reflector, because of the discontinues of materials, particularly for the fields of thermal flux ϕ_2 and the power rate P.

The averaged assembly values of the reconstructed fluxes and power rate are shown in Fig. 7, with which the same conclusions can be drawn. Note that because of the average process, the relative errors in assembly wise are much smaller than that of the pin wise.

More importantly, three main conclusions can be drawn from the prior analysis of the numerical results:

(i) The proposed V-CNN is able to reconstruct the multi-field with observations only from thermal flux;

(ii) The reconstruction errors in assembly wise are far below 5%, which is acceptable for engineering usage, i.e., less than 10%, which is a normal criteria in reactor physics, see [57] for more information;

(iii) Even with a movement of amplitude $\delta = 5$ cm for sensors, the proposed V-CNN is able to reconstruct the field with an error less than 10%.

B. Average performance over a test set

In order to investigate the generalization ability of the field reconstruction method, we analyzed the error performance on 1000 test samples. The error metrics are average relative L_2 error $E(e_2(\phi))$, average relative L_∞ error $E(e_\infty(\phi))$, average relative assembly L_2 error $E(e_2(\phi_{ass}))$, average relative assembly L_∞ error $E(e_\infty(\phi_{ass}))$ and the average SSIM, $E(SSIM(\phi))$, and the standard deviation of the afore mentioned errors.

Table 3 illustrates the numerical results of the errors for the reconstruction of ϕ_1 over the 1000 test samples. All the error metrics present a good agreement between reconstructed field and the original field over the test set. Notice that the worst errors, i.e., the L_∞ errors both in pin wise and assembly wise are below 2%. This good performance is attributed to the smoothness of the fast flux. This is because the fast flux has a relatively longer diffusion length than that of thermal flux, thus the fast flux is less affected by the heterogeneous of materials of this benchmark, see Fig. 6(a) for example.

Table 4 and Table 5 illustrate the numerical results of the errors for the reconstruction of ϕ_2 and P over the 1000 test samples. The average L_∞ errors in pin wise of the thermal flux and the power rate are below 10% when the vibration amplitude is less than 3 cm. Once the amplitude of the vibration gets larger, we will get an average L_∞ error larger than 10%, which in some sense is not acceptable in practical engineering application. On the other hand, if we look the errors in assembly wise, the L_∞ errors are much smaller. The worst case appears for $\delta = 5$ cm when reconstruct ϕ_2, which leads to an error of $E(e_\infty(\phi_{ass})) = 0.0288$ with standard deviation $STD(e_\infty(\phi_{ass})) = 0.0109$. Again, this results confirm the acceptance for engineering application. Notice that though the relative L_∞ errors amount to 10%, most of the points appear around the interface between the fuel and the reflector. The relative large error in this domain is not crucial for safety analysis. To this end, the SSIM indexes in all the three tables are larger than 0.99, which again demonstrate excellent performance for all the field reconstructions.

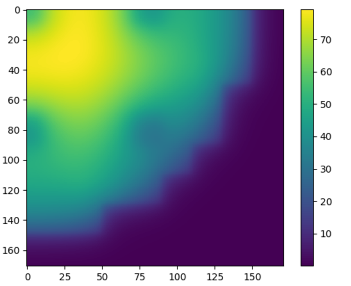

(a) $\phi_{t,1}$

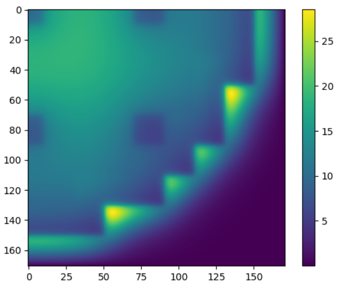

(b) $\phi_{t,2}$

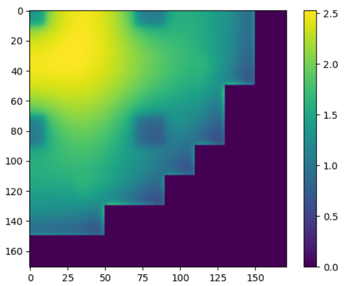

(c) P_t

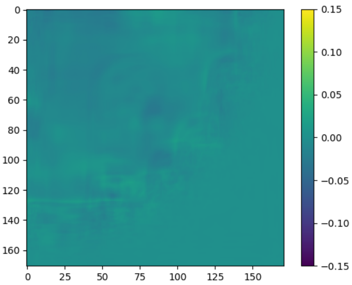

(d) $\frac{\phi_{r,1}-\phi_{t,1}}{\|\phi_{t,1}\|_{L_\infty}}$, $\delta = 1cm$

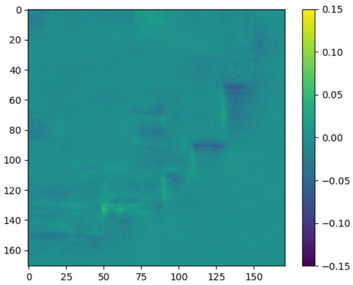

(e) $\frac{\phi_{r,2}-\phi_{t,2}}{\|\phi_{t,2}\|_{L_\infty}}$, $\delta = 1cm$

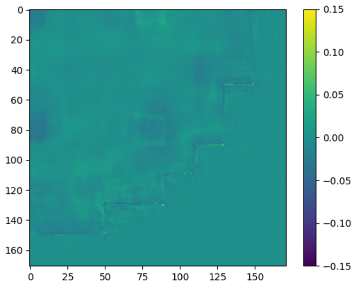

(f) $\frac{P_r-P_t}{\|P_t\|_{L_\infty}}$, $\delta = 1cm$

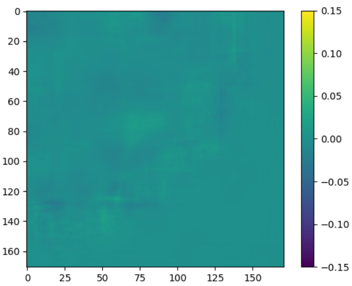

(g) $\frac{\phi_{r,1}-\phi_{t,1}}{\|\phi_{t,1}\|_{L_\infty}}$, $\delta = 3cm$

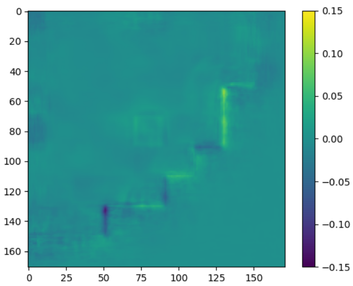

(h) $\frac{\phi_{r,2}-\phi_{t,2}}{\|\phi_{t,2}\|_{L_\infty}}$, $\delta = 3cm$

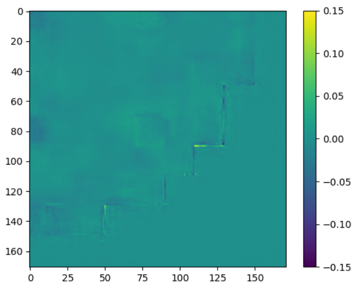

(i) $\frac{P_r-P_t}{\|P_t\|_{L_\infty}}$, $\delta = 3cm$

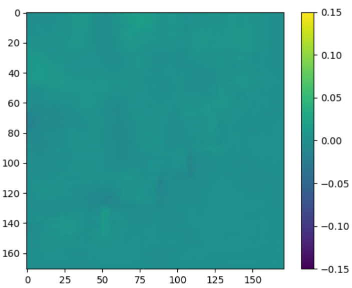

(j) $\frac{\phi_{r,1}-\phi_{t,1}}{\|\phi_{t,1}\|_{L_\infty}}$, $\delta = 5cm$

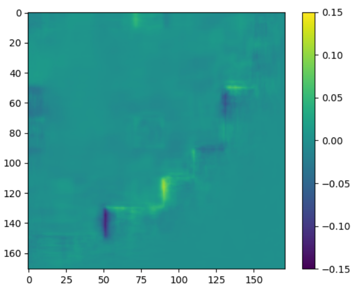

(k) $\frac{\phi_{r,2}-\phi_{t,2}}{\|\phi_{t,2}\|_{L_\infty}}$, $\delta = 5cm$

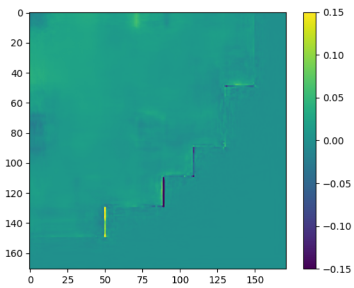

(l) $\frac{P_r-P_t}{\|P_t\|_{L_\infty}}$, $\delta = 5cm$

Fig. 6. The reconstructed fields for different vibration amplitudes, $\delta = 1, 3, 5$ cm for the 2D IAEA benchmark problem.

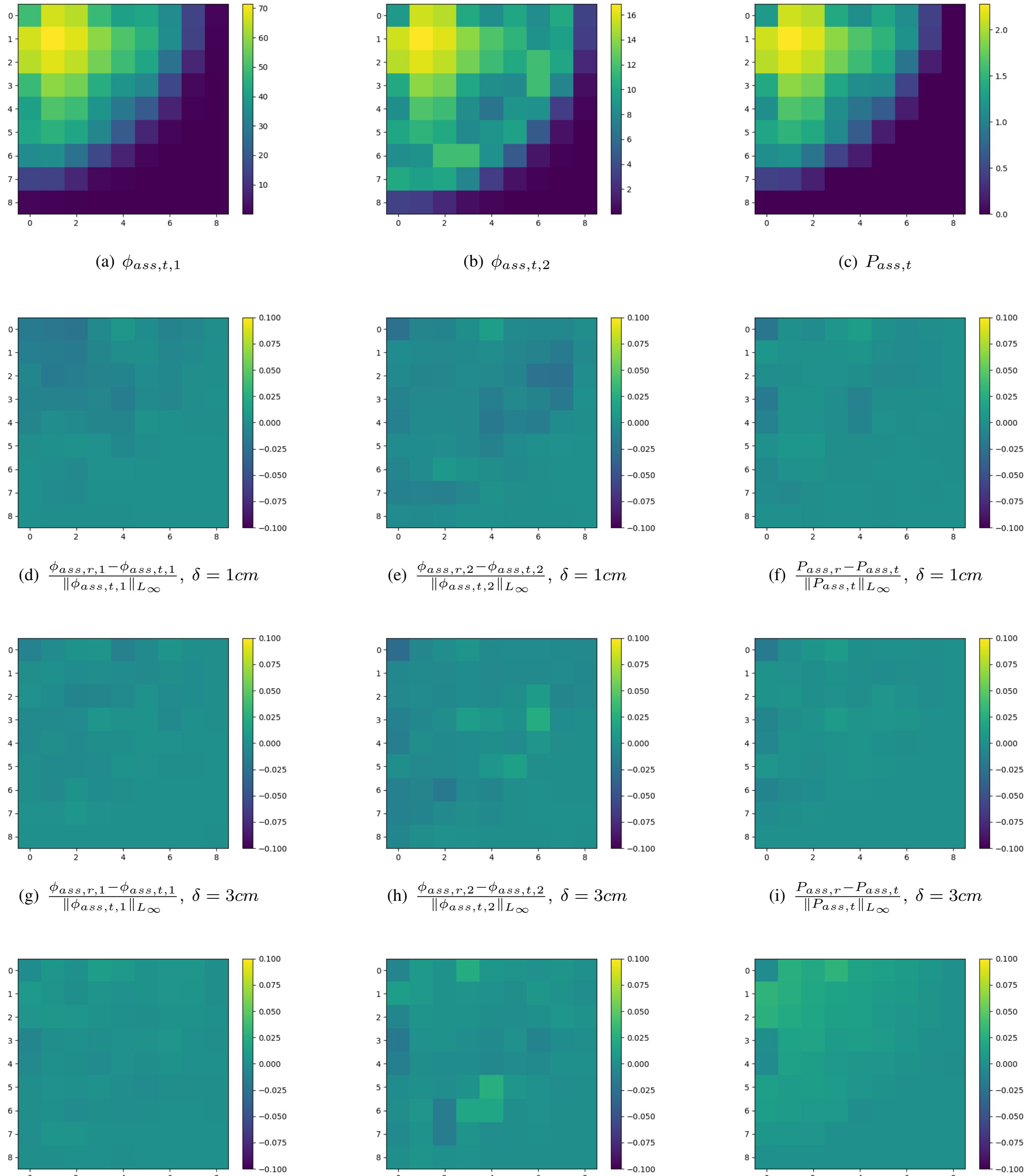

(a) $\phi_{ass,t,1}$ (b) $\phi_{ass,t,2}$ (c) $P_{ass,t}$

(d) $\frac{\phi_{ass,r,1}-\phi_{ass,t,1}}{\|\phi_{ass,t,1}\|_{L_\infty}}$, $\delta = 1cm$ (e) $\frac{\phi_{ass,r,2}-\phi_{ass,t,2}}{\|\phi_{ass,t,2}\|_{L_\infty}}$, $\delta = 1cm$ (f) $\frac{P_{ass,r}-P_{ass,t}}{\|P_{ass,t}\|_{L_\infty}}$, $\delta = 1cm$

(g) $\frac{\phi_{ass,r,1}-\phi_{ass,t,1}}{\|\phi_{ass,t,1}\|_{L_\infty}}$, $\delta = 3cm$ (h) $\frac{\phi_{ass,r,2}-\phi_{ass,t,2}}{\|\phi_{ass,t,2}\|_{L_\infty}}$, $\delta = 3cm$ (i) $\frac{P_{ass,r}-P_{ass,t}}{\|P_{ass,t}\|_{L_\infty}}$, $\delta = 3cm$

(j) $\frac{\phi_{ass,r,1}-\phi_{ass,t,1}}{\|\phi_{ass,t,1}\|_{L_\infty}}$, $\delta = 5cm$ (k) $\frac{\phi_{ass,r,2}-\phi_{ass,t,2}}{\|\phi_{ass,t,2}\|_{L_\infty}}$, $\delta = 5cm$ (l) $\frac{P_{ass,r}-P_{ass,t}}{\|P_{ass,t}\|_{L_\infty}}$, $\delta = 5cm$

Fig. 7. The reconstructed fields in assembly wise for different vibration amplitudes, $\delta = 1, 3, 5$ cm for the 2D IAEA benchmark problem.

Table 3. The errors in different metrics for the reconstruction of ϕ_1 using thermal flux observations from movable sensors.

Width	1	3	5
$E(e_2(\phi))$	0.0097	0.0103	0.0119
$STD(e_2(\phi))$	0.0017	0.0020	0.0031
$E(e_\infty(\phi))$	0.0276	0.0293	0.0303
$STD(e_\infty(\phi))$	0.0078	0.0090	0.0091
$E(e_2(\phi_{ass}))$	0.0084	0.0094	0.0105
$STD(e_2(\phi_{ass}))$	0.0020	0.0022	0.0032
$E(e_\infty(\phi_{ass}))$	0.0155	0.0159	0.0171
$STD(e_\infty(\phi_{ass}))$	0.0046	0.0054	0.0064
$E(SSIM(\phi))$	0.9986	0.9982	0.9979
$STD(SSIM(\phi))$	0.0003	0.0004	0.0004

Table 4. The errors in different metrics for the reconstruction of ϕ_2 using thermal flux observations from movable sensors.

Width	1	3	5
$E(e_2(\phi))$	0.0167	0.0190	0.0213
$STD(e_2(\phi))$	0.0025	0.0032	0.0041
$E(e_\infty(\phi))$	0.0751	0.1001	0.1219
$STD(e_\infty(\phi))$	0.0197	0.0293	0.0391
$E(e_2(\phi_{ass}))$	0.0120	0.0134	0.0141
$STD(e_2(\phi_{ass}))$	0.0025	0.0027	0.0028
$E(e_\infty(\phi_{ass}))$	0.0216	0.0256	0.0288
$STD(e_\infty(\phi_{ass}))$	0.0085	0.0093	0.0109
$E(SSIM(\phi))$	0.9969	0.9964	0.9957
$STD(SSIM(\phi))$	0.0006	0.0008	0.0010

C. Robustness analysis

The robustness of the reconstruction with respect to the number of observations n_{obs} and the amount of training data n_{snapshot} is examined. We show in Fig. 8 the dependence of the relative reconstruction errors in L_2 norm and L_∞ norm on $n_{\text{snapshot}} = 128, 1280, 4096, 8192, 15743$ and on $n_{\text{obs}} = 25, 45, 81$ for recovering thermal flux ϕ_2 over the test set. These numbers of observations $n_{\text{obs}} = 25, 45, 81$ correspond to a sparsity of 0.0855%, 0.154%, 0.277% against the number of grid points over the field. It can be seen from the two figures that the proposed method shows great robustness with respect to the sparsity of sensors and training data. Both low number of observations and low number of training data lead to low-level reconstruction error. Furthermore, the addition of training data improves the reconstruction accuracy much more than the addition of sensors. This result shows that the proposed field reconstruction framework is tolerant of sensor failures, and confirms the potential of real engineering application.

To investigate the robustness of the recovery with respect to the observation noise, we added a noise ϵ_σ randomly sampled in the range $(-\sigma, \sigma)$ to each clean observation y, thus we have the noisy observation $y^o = y(1+\epsilon_\sigma)$ for each sensor. The dependence of the relative reconstruction errors in L_2 norm and L_∞ norm of different noise level, i.e., $\sigma = 0.01, 0.02, 0.03, 0.04, 0.05$ for the recovering of thermal flux ϕ_2 are shown in Table 6. The test is carried out with 81 sensors with vibration amplitude $\delta = 5$ cm. The errors are firstly averaged over 100 repeated random observation samplings for each field reconstruction, and then averaged over the test set. On average, there is a significant change in the reconstruction error once the observation is polluted by noise. The reconstruction error shows a slow linear growth trend with respect to the noise level. Though the L_2 error is below 10%, which is satisfactory for nuclear engineering applications, the L_∞ error still stands around 30%, which is not so satisfactory, provides a direction for further research in diminishing the L_∞ error.

Table 5. The errors in different metrics for the reconstruction of P using thermal flux observations from movable sensors.

Width	1	3	5
$E(e_2(\phi))$	0.0137	0.0164	0.0253
$STD(e_2(\phi))$	0.0031	0.0046	0.0060
$E(e_\infty(\phi))$	0.1429	0.2069	0.2640
$STD(e_\infty(\phi))$	0.0811	0.1079	0.1119
$E(e_2(\phi_{ass}))$	0.0097	0.0108	0.0192
$STD(e_2(\phi_{ass}))$	0.0027	0.0037	0.0058
$E(e_\infty(\phi_{ass}))$	0.0182	0.0191	0.0257
$STD(e_\infty(\phi_{ass}))$	0.0069	0.0081	0.0082
$E(SSIM(\phi))$	0.9951	0.9947	0.9920
$STD(SSIM(\phi))$	0.0012	0.0018	0.0023

Table 6. The dependence of the relative reconstruction errors in L_2 norm and L_∞ norm of noise level σ for the recovering of thermal flux ϕ_2.

Noise level	$E(e_2(\phi))$	$E(e_\infty(\phi))$
0.0	0.0213	0.1219
0.01	0.0493	0.2956
0.02	0.0510	0.2975
0.03	0.0536	0.3013
0.04	0.0572	0.3078
0.05	0.0616	0.3158

V. CONCLUSIONS

In this article, a Voronoi tessellation-assisted convolutional neural networks (V-CNN) is proposed for neutronic fields reconstruction to settle the vibrations of in-core sensors, which may be caused by the aging of operational reactors. The observations from movable in-core sensors are projected to the same global field structure, this projection is achieved with Voronoi tessellation, holding the magnitude and location information of sensors. The general convolutional neural networks were used to learn the map from observations to the global field. Furthermore, the proposed method is able to reconstruct the multi-physics fields e.g., the fast flux, thermal flux and power rate distributions using observations from single field e.g., thermal flux.

Numerical tests based on IAEA benchmark proved its efficiency of the proposed method. Three main conclusions can be drawn from the prior analysis of the numerical results:

(i) V-CNN is able to reconstruct the multi-field with ob-

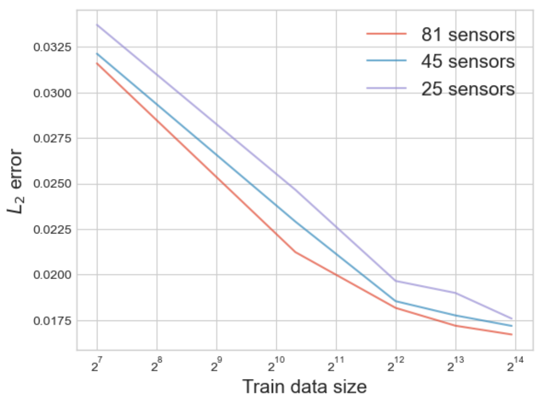

(a) Relative error in L_2 norm

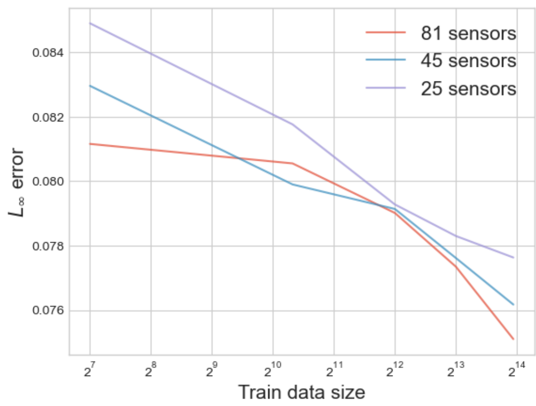

(b) Relative error in L_∞ norm

Fig. 8. The dependence of the relative reconstruction errors in L_2 norm and L_∞ norm on the number of training snapshots $n_{\text{snapshot}} = 128, 1280, 4096, 8192, 15743$ and the number of observations $n_{\text{obs}} = 25, 45, 81$ for recovering thermal flux ϕ_2.

servations only from thermal flux;

(ii) All the reconstruction errors in average are below 5%, which is totally acceptable for engineering usage;

(iii) Even with a vibration amplitude of $\delta = 5$ cm for sensors, V-CNN still performs well.

The original CNN framework is used for image processing, which is now adapted for field reconstruction with rectangular mesh division in this work. For field reconstruction with irregular mesh, an additional mesh mapping is necessary to map the irregular mesh to a rectangular mesh. The adaptability of the proposed method to various reactor configurations would be a continuous work of this article.

This prior study provides a new approach for dealing with field reconstructions with vibration sensors. Future works are possibly to bring out the uncertainty quantification of V-CNN considering observation noise systematically and to push forward to the practical engineering applications based on real nuclear reactors e.g., the HPR1000 reactor developed in China [58]. In this aspect, to evaluate the data uncertainty, the probabilistic neural network [59] or Bayesian neural network [60] could be investigated for a combination of V-CNN; to evaluate the epistemic uncertainty of the model, the Gaussian stochastic weight averaging technique [61] or other techniques could be investigated.

To investigate the adaptability of the proposed method to the HPR1000 reactor, a pin-by-pin wise field calculation is necessary to consider the fuel and sensor vibration, which is now in the process of our group. However, in practical engineering case, the vibrations of reactor components such as fuel and in-core sensors lead to very complex phenomena in the core. Many works [2–6] have been brought to analyze the induced variation of the neutronic fields (also called neutron noise), considering the induced variation of cross-section parameters of the neutron diffusion equations. Inspired by the process of neutron noise analysis, a synthetic modeling approach is also necessary to consider the effects of component vibration. This approach is useful to clarify the interplay or distinctions between the field reconstruction with in-core sensor vibrations and the general reactor noise analysis.

In addition, the combination of V-CNN and fault diagnosis [62] is also a possible research point in the future. With the development of machine learning in the field of nuclear physics [63, 64], adaptions of V-CNN to nuclear physics where CNNs are used [65–67] are also worth trying.

AUTHOR CONTRIBUTIONS

Helin Gong and Sibo Cheng performed research. Helin Gong generated data. Sibo Cheng designed code. Helin Gong analysed data. Helin Gong wrote and revised the paper. Han Li analysed the robustness of the method. All authors reviewed the manuscript.

ACKNOWLEDGMENTS

This research is partially sponsored by the Natural Science Foundation of Shanghai (No.23ZR1429300), and the Innovation Funds of CNNC (Lingchuang Fund). This research is partially funded by the EP/T000414/1 PREdictive Modelling with QuantIfication of UncERtainty for MultiphasE Systems (PREMIERE). This work is partially supported by the Leverhulme Centre for Wildfires, Environment and Society through the Leverhulme Trust, grant number RC-2018-023. The authors are grateful to the three anonymous reviewers' constructive suggestions for the work during the preparation of the manuscript.

COMPETING INTERESTS

The authors declare no competing interests.

[1] IAEA-PRIS, *Nuclear Power Reactors in the World*, Reference Data Series No. 2 (International Atomic Energy Agency, Vienna, 2022).

[2] I. Pázsit and G. T. Analytis, Annals of Nuclear Energy **7**, 171 (1980).

[3] M. Seidl, K. Kosowski, U. Schüler, and L. Belblidia, Progress in Nuclear Energy **85**, 668 (2015).

[4] A. Mylonakis, P. Vinai, and C. Demazière, Annals of Nuclear Energy **155**, 108149 (2021).

[5] A. Vidal-Ferràndiz, D. Ginestar, A. Carreño, G. Verdú, A. Dokhane, V. Verma, Y. Perin, J. Herb, A. Mylonakis, C. Demazière, *et al.*, Annals of Nuclear Energy **177**, 109300 (2022).

[6] P. Vinai, H. Yi, C. Demazière, A. Rouchon, A. Zoia, A. Vidal-Ferràndiz, A. Carreño, D. Ginestar, and G. Verdú, Annals of Nuclear Energy **181**, 109521 (2023).

[7] C. Demazière, P. Vinai, M. Hursin, S. Kollias, and J. Herb, in *Proceedings of the International Conference on the Physics of Reactors–Reactor Physics paving the way towards more efficient systems (PHYSOR2018), Cancun, Mexico* (2018).

[8] S. A. Skidmore and D. J. Krieg (France, 2009) p. 567.

[9] H. Gong, Y. Yu, Q. Li, and C. Quan, Annals of Nuclear Energy **141**, 107346 (2020).

[10] M. Makai and J. Végh, Lecture Notes in Energy **58** (2017), 10.1007/978-3-319-54576-9.

[11] J. Fu, S. Cui, S. Cen, and C. Li, Computer Methods in Applied Mechanics and Engineering **373**, 113516 (2021).

[12] J. Fu, D. Xiao, D. Li, H. R. Thomas, and C. Li, Computer Methods in Applied Mechanics and Engineering **390**, 114532 (2022).

[13] E. Kalnay, *Atmospheric modeling, data assimilation and predictability* (Cambridge university press, 2003).

[14] M. Asch, M. Bocquet, and M. Nodet, *Data assimilation: methods, algorithms, and applications* (SIAM, 2016).

[15] S. Cheng, J.-P. Argaud, B. Looss, D. Lucor, and A. Ponçot, Stochastic Environmental Research and Risk Assessment **33**, 2033 (2019).

[16] O. Goux, S. Gürol, A. T. Weaver, Y. Diouane, and O. Guillet, Numerical Linear Algebra with Applications **n/a**, e2529 (2023).

[17] J.-P. Argaud, B. Bouriquet, P. Erhard, S. Massart, and S. Ricci, Progress in Industrial Mathematics at ECMI 2008 , 401 (2010).

[18] B. Bouriquet, J.-P. Argaud, and R. Cugnart, Nuclear Instruments and Methods in Physics Research Section A: Accelerators, Spectrometers, Detectors and Associated Equipment **664**, 117 (2012).

[19] A. Ponçot, J.-P. Argaud, B. Bouriquet, P. Erhard, S. Gratton, and O. Thual, Annals of Nuclear Energy **60**, 39 (2013).

[20] B. Bouriquet, J.-P. Argaud, P. Erhard, and A. Ponçot, EPJ Nuclear Sciences & Technologies **1**, 18 (2015).

[21] H. Gong, S. Cheng, Z. Chen, Q. Li, C. Quilodrán-Casas, D. Xiao, and R. Arcucci, Annals of nuclear energy **179**, 109431 (2022).

[22] J.-P. Argaud, B. Bouriquet, F. de Caso, H. Gong, Y. Maday, and O. Mula, Journal of Computational Physics **363**, 354 (2018).

[23] H. Gong, Y. Yu, and Q. Li, Nuclear Engineering and Design **370**, 110833 (2020).

[24] R. Fu, D. Xiao, I. Navon, F. Fang, L. Yang, C. Wang, and S. Cheng, International Journal for Numerical Methods in Engineering (2023), https://doi.org/10.1002/nme.7240.

[25] H. Gong, Z. Chen, Y. Maday, and Q. Li, Nuclear Engineering and Design **377**, 111113 (2021).

[26] H. Gong, Z. Chen, and Q. Li, Frontiers in Energy Research **9**, 804018 (2022).

[27] D. Xiao, J. Du, F. Fang, C. Pain, and J. Li, Computers & Fluids **177**, 69 (2018).

[28] S. Riva, C. Introini, S. Lorenzi, and A. Cammi, Annals of Nuclear Energy **190**, 109864 (2023).

[29] S. Riva, C. Introini, S. Lorenzi, and A. Cammi, Annals of Nuclear Energy **190**, 109863 (2023).

[30] S. Cheng, J. Chen, C. Anastasiou, P. Angeli, O. K. Matar, Y.-K. Guo, C. C. Pain, and R. Arcucci, Journal of Scientific Computing **94**, 11 (2023).

[31] C. Introini, S. Cavalleri, S. Lorenzi, S. Riva, and A. Cammi, Computer Methods in Applied Mechanics and Engineering **404**, 115773 (2023).

[32] C. Introini, S. Riva, S. Lorenzi, S. Cavalleri, and A. Cammi, Annals of Nuclear Energy **182**, 109538 (2023).

[33] S. Cheng, C. Quilodrán-Casas, S. Ouala, A. Farchi, C. Liu, P. Tandeo, R. Fablet, D. Lucor, B. Iooss, J. Brajard, *et al.*, IEEE/CAA Journal of Automatica Sinica **10**, 1361 (2023).

[34] Y. Maday, O. Mula, A. Patera, and M. Yano, Computer Methods in Applied Mechanics and Engineering **287**, 310 (2015).

[35] M. S. Terman, N. M. Kojouri, and H. Khalafi, Progress in Nuclear Energy **106**, 300 (2018).

[36] V. Yellapu, A. Tiwari, and S. Degweker, Progress in Nuclear Energy **100**, 326 (2017).

[37] B. Anupreethi, A. Gupta, U. Kannan, and A. P. Tiwari, Nuclear Engineering and Design **366**, 110756 (2020).

[38] N. Karnik, M. G. Abdo, C. E. E. Perez, J. S. Yoo, J. J. Cogliati, R. S. Skifton, P. Calderoni, S. L. Brunton, and K. Manohar, "Optimal sensor placement with adaptive constraints for nuclear digital twins," (2023), arXiv:2306.13637 [math.OC].

[39] K. Fukami, R. Maulik, N. Ramachandra, K. Fukagata, and K. Taira, Nature Machine Intelligence **3**, 945 (2021).

[40] G. Voronoï, Z. Reine Angew. Math **134**, 198 (1908).

[41] F. Aurenhammer, ACM Computing Surveys (CSUR) **23**, 345 (1991).

[42] M. Senechal, Science **260**, 1170 (1993).

[43] A. Okabe, B. Boots, K. Sugihara, and S. N. Chiu, (2009).

[44] R. Venkatesan and B. Li, *Convolutional neural networks in visual computing: a concise guide* (CRC Press, 2017).

[45] S. L. Brunton, B. R. Noack, and P. Koumoutsakos, Annual review of fluid mechanics **52**, 477 (2020).

[46] V. C. Leite, E. Merzari, R. Ponciroli, and L. Ibarra, Nuclear Technology **209**, 645 (2023).

[47] V. Nair and G. E. Hinton, in *Proceedings of the 27th international conference on machine learning (ICML-10)* (2010) pp. 807–814.

[48] D. P. Kingma and J. Ba, arXiv preprint arXiv:1412.6980 (2014).

[49] L. Prechelt, Neural networks **11**, 761 (1998).

[50] S. L. Brunton and J. N. Kutz, *Data-driven science and engineering: Machine learning, dynamical systems, and control* (Cambridge University Press, 2022).

[51] G. H. Blaine R, Froehlich R (Argonne National Laboratory, 1977).

[52] A. Hebert, *Applied Reactor Physics* (Presses inter Polytechnique, 2009).

[53] S. Marguet, *The Physics of Nuclear Reactors* (Springer, 2018).

[54] R. Dautray and J.-L. Lions, *Mathematical Analysis and Numerical Methods for Science and Technology: Volume 6 Evolution Problems II* (Springer Science & Business Media, 2012).

[55] F. Hecht, Journal of Numerical Mathematics **20**, 251 (2012).
[56] Z. Wang, A. Bovik, H. Sheikh, and E. Simoncelli, IEEE Transactions on Image Processing **13**, 600 (2004).
[57] P. An, Y. Ma, P. Xiao, F. Guo, W. Lu, and X. Chai, Nuclear Engineering and Technology **51**, 1721 (2019).
[58] X. Li, Q. Liu, Q. Li, L. Chen, X. Liu, S. Wang, Y. Xie, and Z. Chen, Nuclear Power Engineering S1, **40 S1**, 8 (2019).
[59] R. Maulik, K. Fukami, N. Ramachandra, K. Fukagata, and K. Taira, Phys. Rev. Fluids **5**, 104401 (2020).
[60] L. Sun and J.-X. Wang, Theoretical and Applied Mechanics Letters **10**, 161 (2020).
[61] M. Morimoto, K. Fukami, R. Maulik, R. Vinuesa, and K. Fukagata, Physica D: Nonlinear Phenomena **440**, 133454 (2022).
[62] X.-J. Jiang, W. Zhou, and J. Hou, Nuclear Science and Techniques **34**, 21 (2023).
[63] W.-B. He, Y.-G. Ma, L.-G. Pang, H.-C. Song, and K. Zhou, Nuclear Science and Techniques **34**, 88 (2023).
[64] W. He, Q. Li, Y. Ma, Z. Niu, J. Pei, and Y. Zhang, Science China Physics, Mechanics & Astronomy **66**, 282001 (2023).
[65] H. Zi, Y. Li, Z. Huan, T. Lin, and H. Jianhua, NUCLEAR TECHNIQUES **46**, 030101 (2023).
[66] T. Lin, L. Yong, and T. Yufeng, NUCLEAR TECHNIQUES **46**, 070502 (2023).
[67] Y.-D. Zeng, J. Wang, R. Zhao, F.-P. An, X. Xiao, Y. Hor, and W. Wang, Nuclear Science and Techniques **34**, 79 (2023).
[68] G. Theler, F. Bonetto, and A. Clausse, Actas de la Reunión Anual de la Asociación Argentina de Tecnología Nuclear, XXXVIII (2011).